



LAWRENCE
LIVERMORE
NATIONAL
LABORATORY

In situ observations of reacting Al/Fe₂O₃ thermite: relating dynamic particle size to macroscopic burn time

M. D. Grapes, R. V. Reeves, K. Fezzaa, T. Sun, J. M. Densmore, K. T. Sullivan

May 30, 2018

Journal of Applied Physics

Disclaimer

This document was prepared as an account of work sponsored by an agency of the United States government. Neither the United States government nor Lawrence Livermore National Security, LLC, nor any of their employees makes any warranty, expressed or implied, or assumes any legal liability or responsibility for the accuracy, completeness, or usefulness of any information, apparatus, product, or process disclosed, or represents that its use would not infringe privately owned rights. Reference herein to any specific commercial product, process, or service by trade name, trademark, manufacturer, or otherwise does not necessarily constitute or imply its endorsement, recommendation, or favoring by the United States government or Lawrence Livermore National Security, LLC. The views and opinions of authors expressed herein do not necessarily state or reflect those of the United States government or Lawrence Livermore National Security, LLC, and shall not be used for advertising or product endorsement purposes.

***In situ* observations of reacting Al/Fe₂O₃ thermite: relating dynamic particle size to macroscopic burn time**

Michael D. Grapes^{a*}, Robert V. Reeves^a, Kamel Fezzaa^b, Tao Sun^b, John M. Densmore^a, Kyle T. Sullivan^a

^aMaterials Science Division, Physical and Life Sciences Directorate, Lawrence Livermore National Laboratory, Livermore, CA, USA

^bAdvanced Photon Source, Argonne National Laboratory, Argonne, IL, USA

Keywords: thermite; aluminum; iron oxide; particle size; burn time

Abstract

Time-resolved x-ray imaging is used to capture high-resolution images of the Al/Fe₂O₃ thermite reaction as it proceeds in an extended burn tube. The observed thermite reaction products are generally large, multi-phase composite particles. Image processing algorithms are developed to extract a continuous record of composite particle size as a function of time and distance from the ignition point. Small particles are observed immediately after ignition, followed by a rapid increase in particle size and a gradual decline toward late times. Correlating the dynamic particle size with visible light emission from the reaction, we propose a two-stage mechanism where the combination of early ignition and delayed expansion causes the material closest to the ignition point to undergo substantial coalescence before it begins moving down the tube. We also identify two mechanisms that may contribute to particle size refinement at late times, both based on the collapse of large gas bubbles that are observed preferentially in particles at earlier times. A new approach to extracting burn times from luminous intensity data is explored, and we find that a more nuanced analysis of burn time and luminous intensity may help to improve reactivity assessments when data from *in situ* studies is unavailable.

1. Introduction

Thermite is a reactive material consisting of a physical mixture of a metal fuel and a metal oxide. When they react, they undergo a single-replacement reduction-oxidation reaction in which the fuel is oxidized and the metal oxide is reduced. In a stoichiometric mixture, all of the oxygen required to oxidize

* Corresponding author. E-mail address: grapes2@llnl.gov

the fuel can be obtained from the metal oxide so that, in theory, thermites do not require any ambient oxygen to react. The prototypical thermite reaction is shown in Eq. 1:



Here A is the metal fuel and BO is the metal oxide. As long as the heat of formation of AO is greater than that of BO , the reaction is thermodynamically favorable and liberates heat in the process. Typical thermite heats of reaction range from 2-4 kJ/mol, with adiabatic temperatures often in excess of 3000 K. Fischer and Grubelich have compiled a useful reference of these parameters for many thermite formulations [1].

Thermite formulations are often compared on the basis of “reactivity”. This is a somewhat nebulous term, but can generally be understood as some product of reaction rate and total energy release, i.e. reaction *power*. Thermite reactivity depends on a number of factors. Some of these factors (chemistry, equivalence ratio) affect both reaction rate and total energy release. Others (particle size and distribution, morphology, quality of mixing) have no effect on the theoretical total energy release but play a dominant role in determining the reaction rate. Since the chemistry is often constrained by the specific needs of the application, these *rate-modifying parameters* are often the primary tool used for tuning reactivity. If two formulations are energetically equivalent (e.g. they have the same chemistry and equivalence ratio) and one reacts significantly faster than the other, the faster-reacting formulation is considered “more reactive”. The availability of multiple tunable parameters makes thermite appealing as an engineering material that can be optimized to deliver a precise thermal and/or mechanical energy input. However, in order to realize this potential, experiments are needed that can measure the effects of these parameters on the appropriate length and time scales.

Historically, the reaction “propagation rate” has been one of the most common ways to evaluate thermite reactivity. Thermite is arranged in a nominally 1D geometry and initiated at one end; the speed at which the reaction propagates through the sample is taken as an indicator of reactivity (more reactive thermites propagate faster). Propagation rates are influenced by both chemical reaction kinetics and

thermal transport kinetics. As such, they show the expected trends with parameters affecting the intrinsic reactivity of a formulation like chemistry [2–4] and particle size [5–7] but are also *configuration-dependent*. For example, the same formulation reacted on a block (unconfined) and in a tube (confined) will exhibit vastly different propagation rates [8]. More generally, propagation rate has been shown to depend on factors like equivalence ratio [9–11], architecture [12–14], and packing density [15]. Since these parameters do not primarily affect the intrinsic reaction rate, these variations are instead due to the thermal transport component of the measurement, which is typically dominated by convection [16]. This convolution means that propagation rate is most useful for relative comparisons, and is not an ideal metric to use when attempting to quantify the intrinsic (chemical) reaction rate of the thermite.

Burn time is another metric that has occasionally been applied to thermite reactions [17–21]. While traditionally conceived for metal combustion [22,23] (looking at the “burn time” of individual metal particles), the concept can also be applied to thermites. Here the burn time represents the time it takes to consume an effective volume of reactants at a particular rate. If the reactant volume is invariant (e.g. if it is set by the mixing length scale), the measured burn time will be inversely proportional to the intrinsic chemical reaction rate. Notably, variations in thermal transport kinetics should not affect this measurement, potentially mitigating some of the challenges of 1D propagation experiments. Despite this appeal, there have been relatively few studies to-date exploring burn time in thermites. While some work has found that burn time *is* relatively invariant for a particular formulation [20], other studies still find variations with configuration and/or method of ignition [17–19]. This is generally attributed to differences in the effective reactant volume (e.g. slower ignition heating rates allow more time for particle coalescence).

The interpretation of both propagation rate and burn time measurements can be improved with better information about how the thermite reaction is proceeding at the microscale. Previous efforts to observe the thermite reaction *in situ* have been rather limited in both sample size and duration [24–26].

In this work, we present the first results from an experiment designed to observe thermite reactions at the microscale continuously and over comparatively long timescales (20 – 30 ms). A previously-developed diagnostic tool, the extended burn tube [20], is coupled with time-resolved x-ray imaging for this purpose. As detailed in Sec. 2.2, the extended burn tube is designed to fully contain the products of a thermite reaction and serves to one-directionalize the flow of hot particles, making them easier to image. In previous work [20], it was suggested that thermites in the extended burn tube would undergo so-called “reactive entrainment”, where partially-reacted particles become entrained in the flow of gases generated by the reaction *before* they finish reacting. This would have afforded us the opportunity to track the extent of reaction over time directly at the microscale. Unfortunately, the assumption of reactive entrainment does not appear to be valid, at least for Al/Fe₂O₃ thermite in this experimental configuration. We were, however, able to track the effective particle size of the thermite reactants/products over the course of the reaction and correlate this data with the macroscopic luminous intensity. These results yield new insights into the origins of macroscopic light emission, and allow us to suggest new best practices for how burn time data are extracted from such experiments.

This study focuses on the Al/Fe₂O₃ thermite chemistry, utilizing nanometric fuel and oxidizer particles. This system is of some historical interest since it has been employed for well over a century in the construction and maintenance of railroads [27]. Despite its utility, the Al/Fe₂O₃ reaction is generally considered to be one of the less vigorous thermite reactions [21,24] even though its heat of reaction is comparable to those of Al/CuO, Al/SnO₃, and Al/MoO₃ [1]. This difference in reaction kinetics has been attributed to the fact that Fe₂O₃ does not give up its oxygen very readily early in the reaction [21]. Here, Al/Fe₂O₃ was selected because its longer reaction timescale would maximize our opportunity to observe the reaction *in situ*. However, the experimental technique outlined in this work is applicable to any thermite formulation.

In the sections below, we describe the experimental setup, diagnostics, and timing considerations, and then detail new analysis methodologies that were developed for this work. The paper concludes with an extended results and discussion section exploring the data in detail.

2. Experiment

The basic experimental setup used in this work consists of the extended burn tube, an intense x-ray source (synchrotron), and two high-speed cameras, one for x-ray imaging and one for optical imaging. A schematic is shown in Fig. 1. The experiment was initiated by a button-press, triggering the high speed cameras and the thermite igniter. The fast shutter controlling entry of the x-ray beam was opened 70 – 120 ms after experiment start to account for the thermite ignition time and the time required for particles to travel down the tube to the measurement position. The sections below give additional details on each component of the experiment.

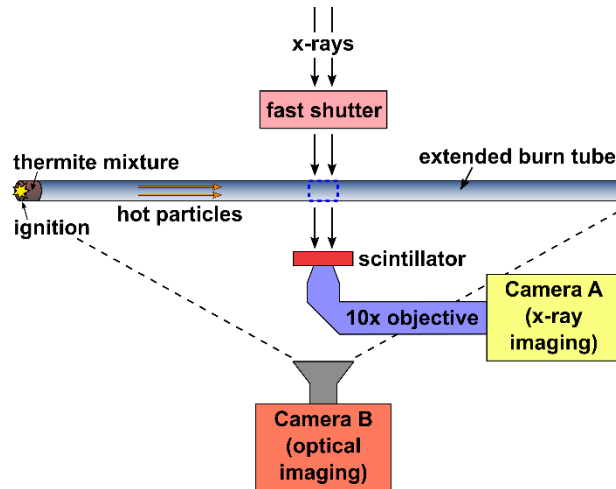


Fig. 1. Schematic depiction of the experimental setup for *in situ* x-ray imaging at APS Sector 32. The burn tube at center is loaded with thermite at one end and confines the flow of hot particles in one direction. X-rays pass through the tube and strike a scintillator which is imaged by a high-speed camera (A). A second high-speed camera (B) is set back from the burn tube and captures optical images of the experiment.

2.1 Extended Burn Tube

The extended burn tube experiment has been described in detail previously [20]. In brief, the objective of this experiment is to match the total volume of the burn tube to the anticipated volume of the reaction products. This allows the reaction to expand and proceed to completion entirely within the tube.

The tube used in the experiments reported here had an inner diameter of 6.35 mm, a wall thickness of 3.2 mm, and a length of 1.2 m. One end of the tube was capped and fitted with a nichrome igniter coil. To minimize adhesion of the thermite to the walls of the tube during loading (due to electrostatic interactions), a 15 cm “load tube” was cut and attached to a rail. The cap and nichrome igniter were affixed to one end of this tube, and a 100 mg thermite charge was added using a funnel. The tube was tapped lightly until all of the thermite was consolidated at the igniter end. The resulting thermite charge occupied less than 1 cm of the tube length. The loaded tube was then mated with a second 1.05-m-long tube, and the two pieces were taped together to yield the full 1.2 m length. The tube was placed in the path of and perpendicular to the synchrotron beam as shown schematically in Fig. 1. To initiate the experiment, the thermite was ignited by flowing current from a DC power supply (ZUP36-24, TDK-Lambda, Inc.) through the nichrome wire. Upon ignition, gas generated by the thermite reaction propelled hot particles down the tube. These were observed using the x-ray imaging high-speed camera, and also generated a visible luminous streak that was recorded by the optical high-speed camera.

2.2 X-ray Imaging

Experiments were performed at beamline 32-ID of the Advanced Photon Source at Argonne National Laboratory. The beam passed through a fast shutter to define the total exposure time of the experiment (approximately 50 ms), then through the tube and hot particles, and finally struck a scintillator detector on the far side of the burn tube. The x-ray exposure time was limited to avoid overheating the scintillator. See Fig. 1 for a schematic depiction of this layout. The scintillator was imaged through a 10x magnifying objective by a high-speed camera (Photron FASTCAM SA-Z), shown as Camera A in Fig. 1, at a frame rate of 20,889 fps and a resolution of 1000 x 1024. With the camera’s 20 μm x 20 μm pixels, the 10x objective gave an image pixel size of 2 μm x 2 μm and an effective viewing area of 2.000 mm x 2.048 mm. To observe reacting particles at different times after ignition, the tube was translated

perpendicular to the x-ray beam. A total of five measurements were taken, at distances of 2.5 cm, 10 cm, 20 cm, 30 cm, and 60 cm from the ignition point.

Since the reacting thermite particles travel down the tube at very high speeds, these experiments were performed in the Advanced Photon Source's "hybrid-singlet" mode to maximize the temporal resolution. In this configuration, rather than distributing beam current evenly over all of the electron bunches in the synchrotron storage ring, a single, high-current (16 mA) bunch is created and offset temporally from the remaining 88 mA of beam current (distributed in 56 smaller bunches) [28]. By synchronizing the camera to image with the 16-mA "singlet" bunch only (average duration ~50 ps) much sharper images were obtained than would have been possible integrating over multiple smaller bunches. The repetition rate of the singlet pulse is approximately 271 kHz, while the maximum frame rate of the camera is 21 kHz at full resolution (1000 x 1024 pixels). As a consequence, images were acquired with every 13th singlet, yielding the unique 20,889 fps frame rate.

2.3 Optical Imaging

The luminous streak generated by the travel of hot thermite particles down the tube was captured by optical high-speed imaging of the experiment (Camera B in Fig. 1). A Phantom Miro 110 high-speed camera (Vision Research) fitted with a Tokina ATX-PRO 11-16 mm wide-angle lens was used. The frame rate was 10,000 fps for all experiments.

2.4 Materials

Al/Fe₂O₃ thermite was formulated by combining Al (80 nm average particle diameter, Novacentrix) and Fe₂O₃ (≤50 nm particle diameter, Aldrich) powders in a ratio of 32% Al to 68% Fe₂O₃ by weight, corresponding to a stoichiometric equivalence ratio of 1 after accounting for the fact that the nano-Al powder is only 73% elemental Al by mass. The combined powders were mixed (dry) in 500 mg batches using a resonant acoustic mixer (Resodyn LabRAM I) at 100 g of acceleration for 12 minutes.

These conditions were found to give consistent performance, while exceeding this mixing time yielded no additional reduction in burn time.

3. Analysis

Analysis “time zero” was set at the time of first light from the reaction, as measured by the optical high speed camera. All plots of luminous intensity or particle size shown in the sections that follow use this convention.

3.1 X-ray Image Processing

This section summarizes the routines used to analyze x-ray images and extract quantitative measurements from them. All of the batch image processing described in this section was performed with ImageJ version 1.50 [29]. While conceptually simple, the specific implementation details of these routines are beyond the scope of a scientific paper. In lieu of including these details, the ImageJ scripts used to process the images are available from the corresponding author upon request.

The main source of contrast in the x-ray images is absorption (mass/thickness). As such, the images consist of dark particles on a light background as shown in Fig. 2a. This image also contains significant variations in background intensity and persistent defects like light/dark pixels, bright spots, and vignetting (darkness in the corners) from the imaging optics. While the human eye is quite adept at extracting information (i.e. particles) from noisy images like Fig. 2a, these background features must be removed before a computer can perform this task.

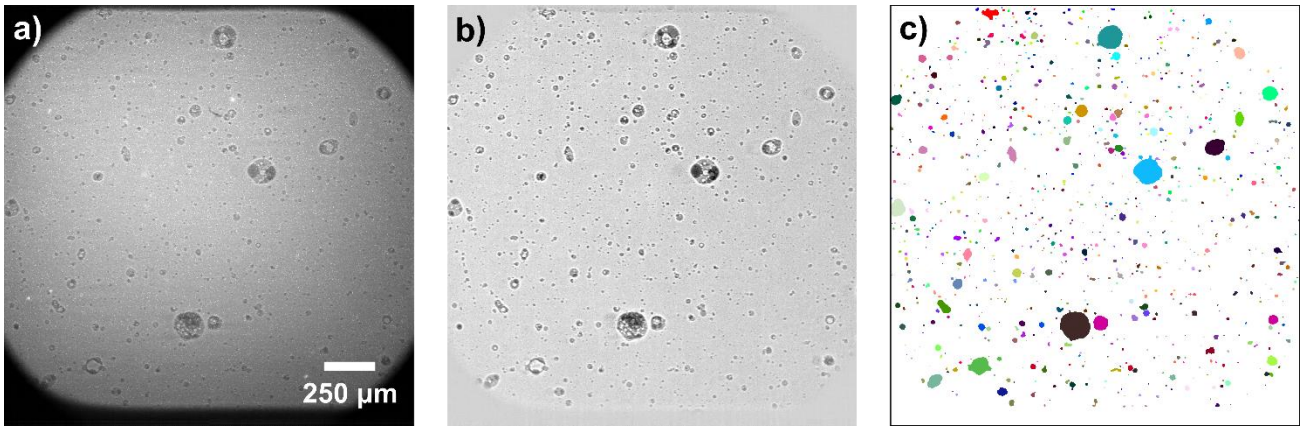


Fig. 2. Example x-ray image after varying levels of processing: (a) raw image, (b) the same image after 199-frame moving-average background subtraction, and (c) the same image after threshold segmentation and particle analysis (each particle colored randomly for clarity).

Fig. 2b shows the same image after a 199-frame (9.53 ms) moving-average background subtraction. In this process, multiple frames around the image of interest are averaged to obtain a background image. This works because most of the background features identified in Fig. 2a are immobile and appear in every frame. In contrast, the particles are moving and change in every frame. By taking an average of many frames, the static features (background) are reinforced while the features of interest (particles) are ignored. The moving average accounts for time-dependent variations in background due to the changing response of the x-ray scintillator as it heats up. The number of frames in the average is a balance between rejecting particles and tracking the change in background: too few and shadow negatives of particles are observed, too many and there will be unacceptable non-uniformity in the background. A width of 199 frames was found to be a good compromise for this data.

After background subtraction, the image must be “segmented” to determine what is a particle and what is background. This can usually be done by specifying a threshold intensity and splitting the image between dark and light areas. However, the optimal threshold value differs for each image, and it is a non-trivial problem to find this optimal threshold automatically. A number of algorithms have been developed to address this problem. Of those tested, the best results were obtained using Huang’s fuzziness minimization method [30] as implemented in ImageJ. Fig. 2c shows the result of applying this threshold to the image in Fig. 2b. Once a binary image like Fig. 2c is obtained, it is trivial to extract a population

of “particles” and quantify their size and shape. This was done using ImageJ’s standard “Analyze Particles...” routine.

3.2 Particle Size Statistics

The direct result of applying particle size analysis to a binary image like Fig. 2c is a list of size and morphology metrics for *every* particle in the image (973 of them in the case of Fig. 2). This level of granularity is excessive for a single image, let alone the hundreds of such images that make up a single x-ray imaging sequence. To reduce the raw particle measurements down to something more meaningful, a representative particle size was computed for each image. This process started by computing the effective diameter of each particle in the image. While particle analysis can yield many different measurements of size and shape, we restricted consideration to the total projected area of each particle, A_p . This is just the number of pixels belonging to each particle multiplied by the area of one pixel ($4 \mu\text{m}^2$). Assuming a spherical geometry, a particle’s effective diameter can be calculated as:

$$D_{\text{eff}} = 2 \sqrt{\frac{A_p}{\pi}} \quad (2)$$

While not all particles are spherical, some assumption must be made and the general scaling law $L \propto \sqrt{A}$ should be valid regardless.

From the population of all particles in the image, we then calculated a single representative particle size: the volume-weighted median particle diameter, \tilde{D}_3 . Intuitively, the volume-weighted median particle diameter is the diameter of a particle that splits the *volume* of particles in the image into two: 50% of the total volume in the image is made up of particles smaller than the median, and the other 50% is made up of particles larger than the median. Mathematically, \tilde{D}_3 was computed by (1) calculating the effective volume of each particle ($V = \pi D_{\text{eff}}^3/6$), (2) sorting the volumes in ascending order, (3) computing a cumulative sum, (4) identifying or interpolating the volume that split the cumulative sum into two equal halves (the median *volume*), and then (5) converting the median volume back to an effective particle

diameter. Compared to the unweighted median, the volume-weighted median is much more sensitive to the large particles in an image. To illustrate, the volume-weighted median particle diameter for the image in Fig. 2 is 88.9 μm , while the unweighted median particle diameter is just 9.76 μm . While both measurements are valid measures of central tendency, the volume-weighted median better reflects the perceived particle size and correlates better with the macroscopic optical emission from the experiment, which is expected to scale with volume [17,31].

The final step was to smooth the data temporally. This helped to reduce experimental variability and decrease the sensitivity of the results to outlier particles. Smoothing was performed using a 15-point 50% “percentile filter”, which mapped each data point to the median value of a window of 15 points around it. The smoothing operation was implemented in OriginPro 2016 (OriginLab).

3.3 Luminous Intensity and Burn Time

The optical high-speed camera (Sec. 2.3) recorded the experiments in RGB color. For intensity analysis, the videos were converted to grayscale using “lightness” as defined in the HSL (hue-saturation-lightness) color space. This is the average of the largest and smallest color components in each pixel, i.e.

$$L = \frac{1}{2}(M + m) \quad (3)$$

where L is the lightness, M is the largest color component, and m is the smallest color component.

Typically, burn time is measured in experiments where the volume of thermite is relatively small and constant [17,18,21]. In contrast, in the extended burn tube the volume occupied by thermite expands 10 – 100x during the experiment [20]. It is inappropriate to compute the average intensity using a global frame average since the number of pixels occupied by thermite changes in each frame. Rather, the average intensity should be computed only over the portion of the tube currently occupied by thermite. To implement this in an automated way, a “hot pixel” average was used. This includes in the average only those pixels that exceed a threshold intensity and naturally accounts for the changing volume of thermite as long as the entire volume remains above the threshold intensity. Global and hot pixel intensity plots

are compared in Fig. 3a. The hot pixel (volume-normalized) intensity peaks earlier and decays faster than the global average. The global average changes more slowly because it is “weighed down” by the large fraction of pixels that don’t contain thermite.

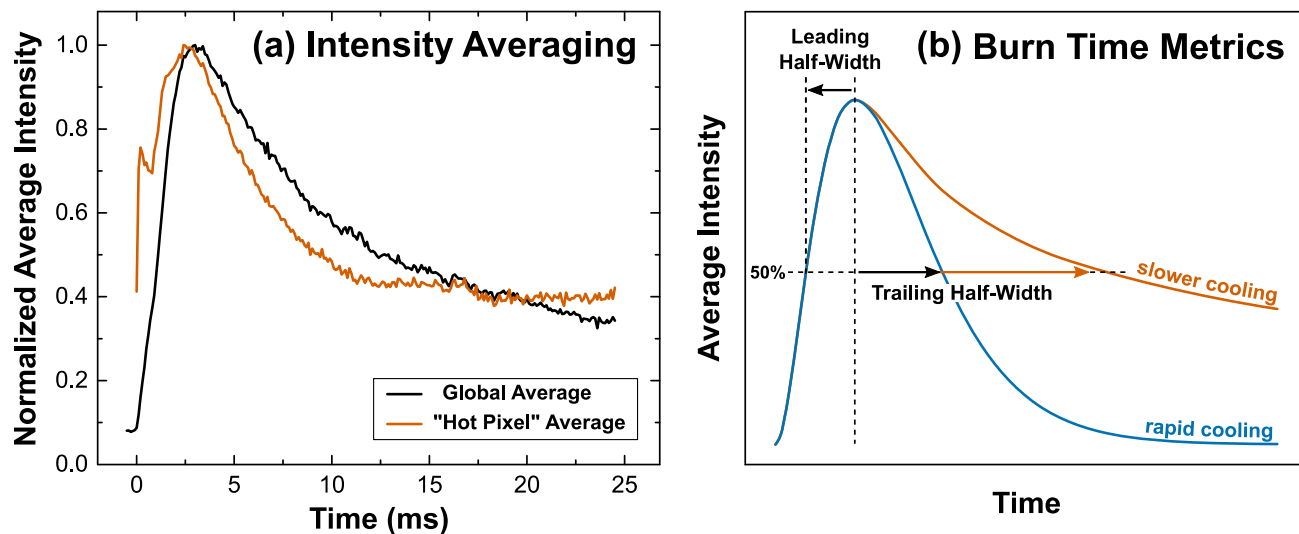


Fig. 3. Illustration of intensity averages and burn time metrics: (a) example of experimental data showing the difference between global and “hot pixel” intensity averages, and (b) schematic illustration of leading and trailing half-width measurements for two intensity curves with different cooling rates.

From an intensity versus time measurement, burn time is typically extracted by measuring the width of the intensity peak at a given fraction of the maximum, e.g. 50% or 10%. The 50% measurement, commonly referred to as the full-width at half-maximum (FWHM), is a simple, intuitive way to quantify “burn time”. However, it is most useful for describing symmetric peaks, while luminous intensity data is often skewed as shown in Fig. 3a. Using a FWHM alone to describe skewed data can mask potentially valuable information about the time-dependence of a reaction. To improve on this shortcoming, we have deconstructed the FWHM into two components: a *leading* half-width and a *trailing* half-width. The leading half-width is measured from the peak intensity to the 50% level on the left, while the trailing half-width is measured to the same level on the right. The sum of the two half-widths is the standard FWHM, but having separate values gives additional information on the shape of the peak. If the leading component is larger than the trailing component the data is skewed left, while if it is smaller the data is skewed right. If the two half-widths are equal the peak is symmetrical.

Fig. 3b illustrates these new measurements for two schematic intensity-versus-time curves. The curves are drawn to highlight one possible variation in real data, where the time to reach the peak intensity changes little but the time it takes for the intensity to decay changes a lot. A conventional FWHM burn time measurement would indicate that the experiment with slower cooling kinetics had a longer burn time, but would give little insight into the origin of the difference. By reporting separate leading and trailing half-width burn times, we arrive at a more nuanced interpretation of the data: the leading half-width is essentially identical (suggesting similar kinetics) while the trailing half-width is responsible for most of the variation in FWHM burn time (suggesting a difference in cooling kinetics due to, for example, particle size or ambient temperature).

4. Results and Discussion

The measurements and analysis procedures detailed above result in several distinct data streams, in addition to the raw images of reacting particles. In the sections that follow, we introduce the reader to the data and explore some of the more interesting features.

4.1 Overview

A montage of an experiment as observed by optical high-speed camera is shown in Fig. 4. The first frame shown is from 0.5 ms after ignition; ignition itself (not shown) occurs at $t = 0$. As time passes (moving down in the figure) hot thermite particles are observed expanding down the tube. The light emitted separates into two distinct zones prior to 8.0 ms: a leading zone (Zone 1) and a trailing zone (Zone 2). The leading zone appears to outpace the trailing zone, but also disappears much earlier. The persistent trailing zone eventually transitions from a continuous bright cloud to discrete bright areas, suggesting the presence of large, hot particles. These particles persist for the entire time shown in the figure (20 ms) and in fact through the end of the full video (47.3 ms).

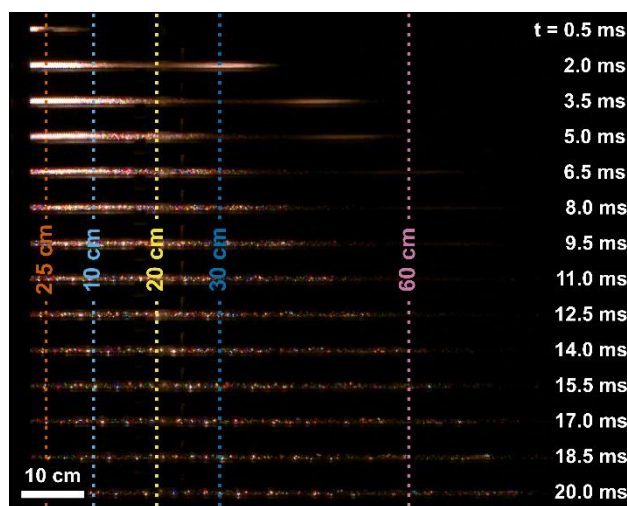


Fig. 4. Optical high-speed video montage of the Al/Fe₂O₃ extended burn tube reaction. Ignition occurred on the left side of the frame at $t = 0$. The positions of the five *in situ* x-ray measurements are shown (dashed lines). The full high-speed video of this experiment is available as supplemental information.

When each frame in the video summarized by Fig. 4 is processed to yield its hot pixel average intensity (see Sec. 3.3), a plot of average intensity versus time is obtained as shown in Fig. 5. As above, $t = 0$ is the ignition point. While the plots are color-coded by x-ray measurement position for completeness, Fig. 5 gives no information about the spatial distribution of intensity; rather, it represents the average global intensity of *all* the thermite in the tube. The data are heavily skewed to the right, indicated by a trailing half-width ($9 \text{ ms} \pm 2 \text{ ms}$ [avg. \pm std. dev., $n = 5$]) that is significantly longer than the leading half-width ($2.7 \text{ ms} \pm 0.8 \text{ ms}$ [avg. \pm std. dev., $n = 5$]). The peak intensity is reached only $2.8 \text{ ms} \pm 0.7 \text{ ms}$ (avg. \pm std. dev, $n = 5$) after ignition, corresponding to the second or third frame of Fig. 4. If the leading half-width is taken as an indicator of the duration of the primary exothermic reaction, Fig. 5 suggests that most of the x-ray data acquired in the experiments shows not the reaction itself but its aftermath.

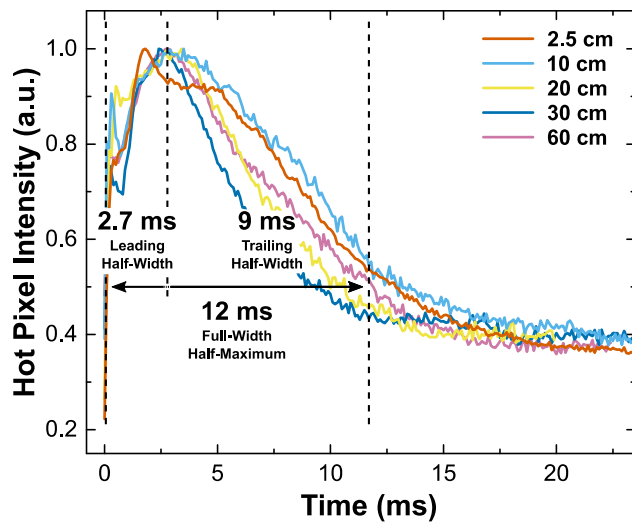


Fig. 5. Normalized average intensity vs. time curves for all five experiments. The average intensity was calculated using a hot pixel threshold of 10 (see Sec. 3.3). The average full-width at half-maximum (12 ms) is indicated, along with the leading half-width (2.7 ms) and trailing half-width (9 ms) components. The uncertainty in the averaged values is omitted from the figure for clarity; see text for details.

As the thermite expands down the tube, it passes the x-ray measurement positions shown in Fig. 4. Full video records of the x-ray images recorded at each position are available as supplementary information. Fig. 6 shows plots of volume-weighted median particle diameter (see Sec. 3.2) versus time measured at each of the five x-ray measurement positions. Again, the data are aligned so that ignition is at $t = 0$. Note that in this case, each data trace starts at a different time. The delay reflects the time it takes for particles to travel down the tube and reach the measurement position. For example, Fig. 6 indicates that no particles pass the 60-cm measurement position until approximately 5 ms after ignition. This is consistent with our visual observations of the burn tube in Fig. 4. The maximum and half-maximum intensity times from Fig. 5 are indicated by the dashed vertical lines in Fig. 6.

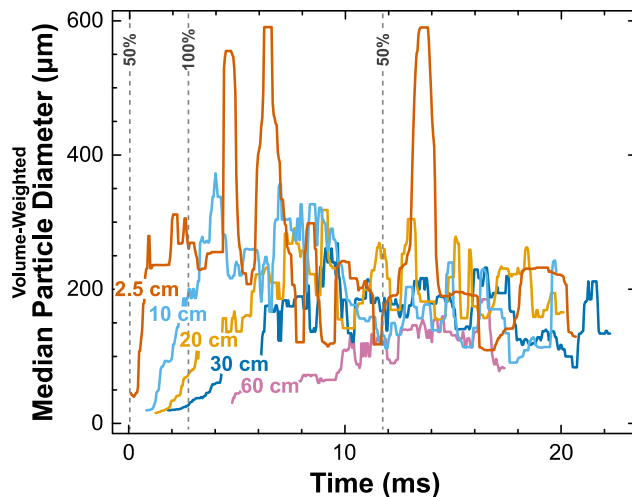


Fig. 6. Smoothed, volume-weighted median particle diameter versus time measured at five different distances from the ignition point. Ignition occurs at $t = 0$, but particles reach each measurement position at a different time. The vertical dashed lines show the correspondence between the particle size and the luminous intensity levels shown in Fig. 5 (100% and 50% are the maximum and half-maximum levels, respectively).

All five of the measurement positions show the same pattern of a small starting particle size, a ramp up to a larger particle size, and a gradual decay thereafter. They are similar because they all measure the same thermite cloud (within shot-to-shot variation). The differences arise because each measures the cloud at a different time after ignition. In particular, the slope of the initial particle size ramp decreases from the earliest measurement (2.5 cm) to the latest (60 cm), implying an initially sharp change in particle size that broadens over time because small particles move faster than large particles. The peak particle size also decreases as time proceeds. By the time the cloud reaches the 60-cm measurement position, the maximum particle size is only about half of what it was at 2.5 cm. This implies some sort of particle refinement mechanism acting on the thermite.

4.2 Particle Morphology, Composition, and Size

Fig. 6 shows that the particles observed traveling down the tube are orders of magnitude larger than the nanopowders used in the initial formulation. One might expect that such particles are highly agglomerated, multi-phase composites, and in general this is the case. Fig. 7 shows an example, captured at the 10-cm measurement position about 8.8 ms after ignition. The scale is impressive: the large particle

in Fig. 7 is more than 800 μm in diameter, and several other particles larger than 200 μm are also visible. Even the “small” particles in the image are 20 – 30 μm in diameter, still more than an order of magnitude larger than the starting nanopowders. While individual nanoparticles are below the resolution of the imaging system, given the prevalence of large particles and the volume of material contained in them it seems as though few, if any, nanoscale particles remain at this point in the reaction.

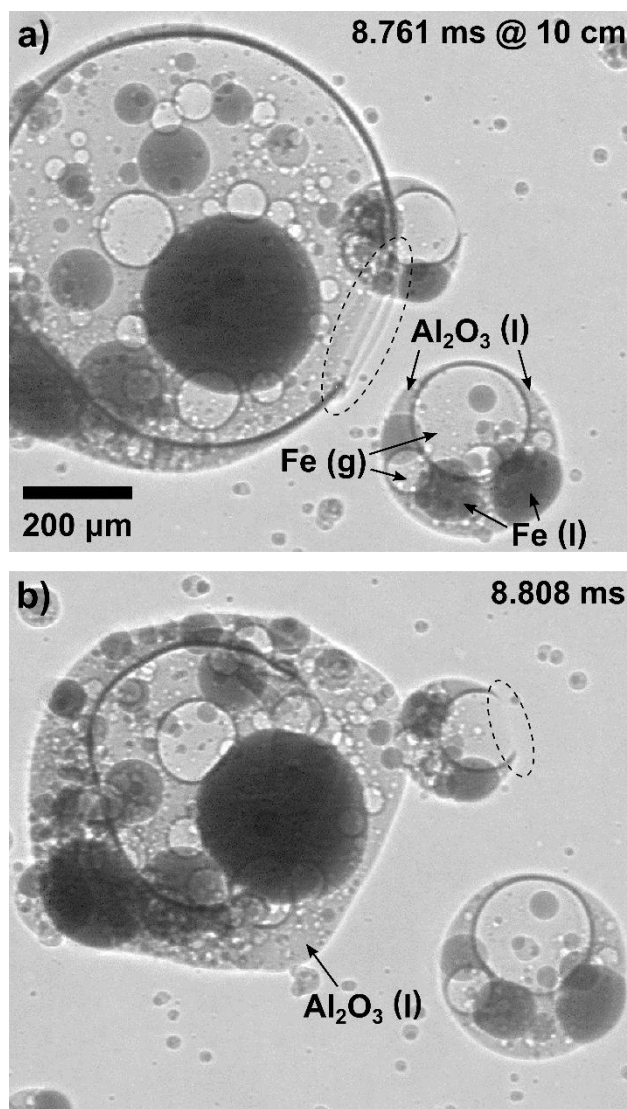


Fig. 7. Two consecutive images showing large, multi-phase particles. These particles are representative of what is observed at the first three measurement positions over the first 10 – 20 ms after ignition. These images were captured at the 10-cm measurement position at 8.761 ms (a) and 8.808 ms (b).

Within the large particles in Fig. 7, brightness variations suggest the presence of several discrete phases. While there are a multitude of brightness shades (particularly in the largest particle), much of this

variation can be explained by the different sizes of sub-phase and most likely does not indicate a multitude of compositions. Rather, we identify three main phases (labeled in one of the smaller particles of Fig. 7a for clarity): a very dark (strongly absorbing) phase, a very light (weakly absorbing) phase, and a gray (moderately absorbing) phase. The darkest and lightest phases appear as spherical deposits in a matrix of the gray phase. The gray phase is difficult to see in the largest particle in Fig. 7a because it is observed through a very large bubble of the light phase. In Fig. 7b, the large bubble has disappeared and the gray matrix phase is much more visible as labeled. The rapid disappearance/shrinkage of the light phase from Fig. 7a to Fig. 7b suggests that it is a vapor phase. The other two phases appear to be molten condensed phases on account of their generally spherical geometry and response to deformation. Since these images were captured well after the time of peak luminous intensity (2.8 ms), it seems most likely that they are reaction products. This would make the dark phase elemental Fe and the gray matrix phase Al_2O_3 . The vapor phase could be entrapped air, gaseous oxygen (an intermediate product from decomposition of Fe_2O_3), or gaseous iron (an expected final reaction product). Given that the initial mixture was stoichiometric, there should not be substantial excess oxygen present with the reaction products. Thus the most likely candidate for the vapor phase is elemental iron. Assuming equilibrium between iron liquid and vapor, this puts the temperature of the large particles at the boiling point of iron, 2862 °C, consistent with the predicted adiabatic temperature of the Al/ Fe_2O_3 reaction [1]. Al_2O_3 should also be molten at this temperature.

To further evaluate these phase assignments, consider the expected volume of each reaction product. In equilibrium [1], the products of a perfect stoichiometric mixture are expected to be 47.7 wt% Al_2O_3 liquid, 44.4 wt% Fe liquid, and 7.8 wt% Fe vapor. Including the contribution of the initial Al_2O_3 in the nano-Al shell, these values become 52.2 wt% Al_2O_3 liquid, 40.6 wt% Fe liquid, and 7.2 wt% Fe vapor. At 2862 °C, the estimated density of molten Al_2O_3 is about half that of molten Fe [32,33]. Consequently, the condensed products consist of 72.5 vol% Al_2O_3 liquid and 27.5 vol% Fe liquid. An

excess of Al_2O_3 is consistent with the dark phase being Fe and the gray phase being Al_2O_3 , since the dark phase is observed dispersed in the gray phase. Incidentally, the relatively small mass fraction of vapor still constitutes 100 – 1000 times (depending on pressure) more volume than all of the condensed products combined. Since the volume of entrapped gas (light phase) appears to be comparable to that of molten Fe (i.e. quite small), it seems that by far the majority of the gas generated by the reaction is *not* entrapped at this point and instead surrounds the particles, propelling them down the tube.

The three large particles in Fig. 7 exhibit a marked similarity in structure despite their varied sizes. Each features one especially large gas bubble which tends toward one side of the particle, yielding a lopsided particle with more of the condensed phases opposite the large bubble. These large bubbles have a tendency to “pop” or escape the particle, effectively shrinking the particle. Fig. 7a captures the moment right before this occurs in the largest particle – the dashed oval highlights where a circular hole has opened in the molten shell of the bubble. In the next frame, 47 μs later, the bubble (and particle) has shrunk considerably due to expulsion of vapor. This shrinkage continues in the subsequent frame (not shown). Fig. 7b captures the start of the same phenomenon in the smaller particle at upper right. Again, a dashed oval shows the clear thinning of the outer shell of the particle. In the next frame (not shown) this particle also shrinks considerably.

Fig. 6 indicates that the median particle size decreases as the particle cloud evolves over time. Observations of the particles in the tube indicate that as they shrink, they also become less multi-phase and eventually solidify. Fig. 8 shows an example, collected from the 60-cm measurement position 14.218 ms after ignition. While there is still a mix of large and small particles, here the smaller particles make up a larger volume fraction of the total image ($\tilde{D}_3 = 160 \mu\text{m}$ for Fig. 8 versus $\tilde{D}_3 = 544 \mu\text{m}$ for Fig. 7). The large particles still appear to contain two phases, but their more irregular exterior surfaces suggest they are now solid rather than molten. The smaller particles overwhelmingly consist of the gray phase identified previously (likely Al_2O_3).

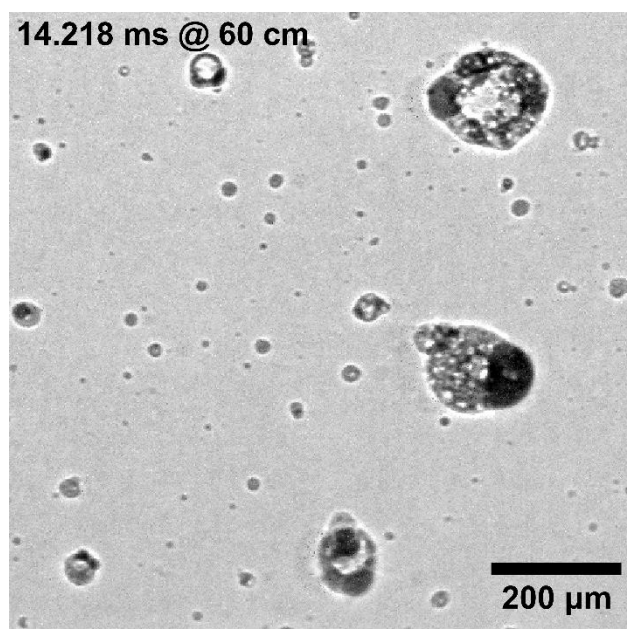


Fig. 8. X-ray image showing representative late time particles, captured at the 60-cm measurement position 14.218 ms after ignition. The large, multi-phase particles are not nearly as large as in Fig. 7, and their irregular exteriors suggest they are now solid. The more abundant small particles are predominantly single-phase (Al_2O_3).

While the larger, solid multi-phase particles observed in Fig. 8 seem like the logical end result of the bubble-popping mechanism shown in Fig. 7, that mechanism is insufficient to explain the many small, single-phase particles observed. These particles cannot have reacted at this length scale since the other product is missing, so there must be an additional particle size refinement mechanism driving the creation of such particles after the reaction is complete. Fig. 9a shows a second phenomenon that might offer an explanation. As in Fig. 7, the process starts with the collapse of a large gas bubble. Here, however, the recoil of the particle after collapse results in a jet of molten material, which then reduces its surface energy by pinching off into multiple smaller particles (Plateau-Rayleigh instability). These small pinched off particles may be the single-phase particles observed in Fig. 8. It's important to note that the jet is a secondary effect produced *after* the gas bubble collapses, and does not indicate that the bubble itself contained molten material. Interested readers are referred to the corresponding segment of the x-ray imaging video in the supplemental materials. The jet is predominantly Al_2O_3 , consistent with the observation that most of the small particles are single-phase Al_2O_3 . In addition, this mechanism was observed with surprising frequency given the small fraction of the reaction sampled (Fig. 9b shows

multiple examples). If it occurs with this frequency throughout the particle cloud, it could reasonably be responsible for the majority of the small product particles observed.

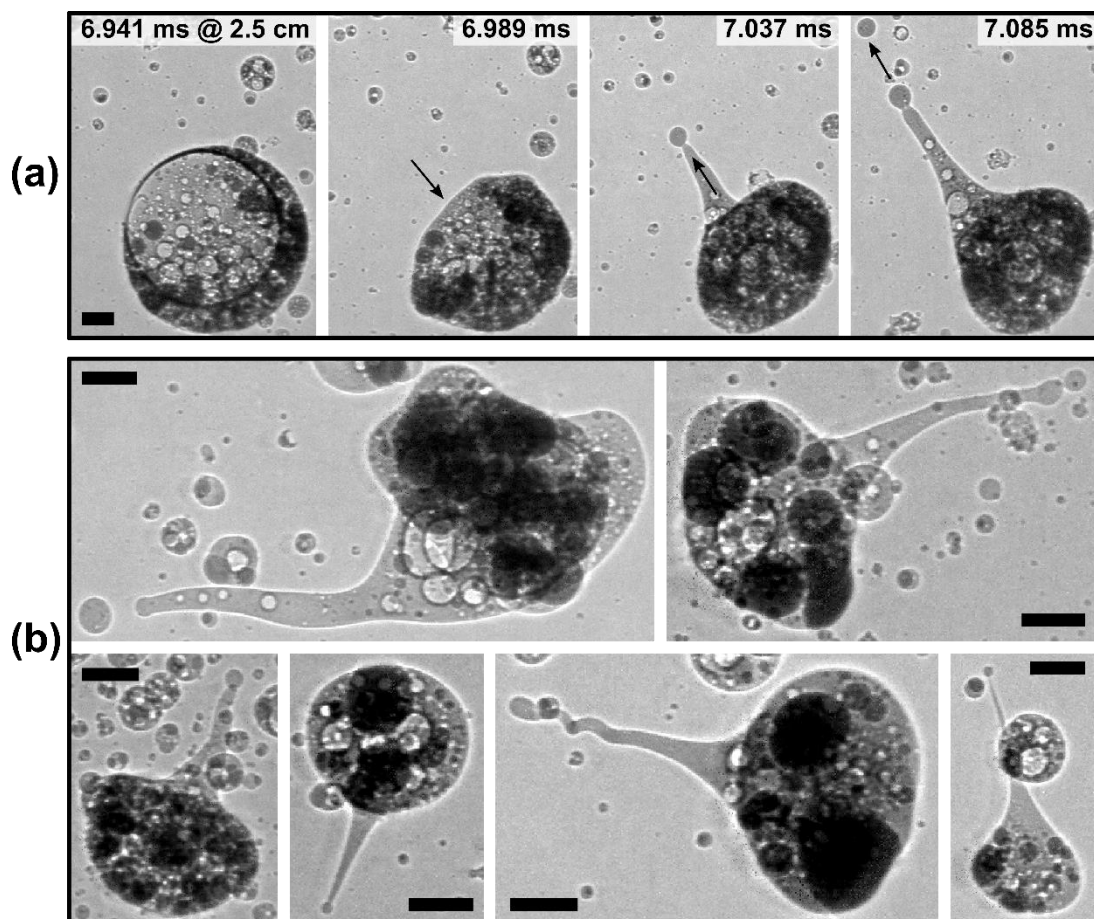


Fig. 9. X-ray images showing how bubble collapse can generate small, single-phase particles. Particle flow is to the right. The scale bar is 100 μm long in all images, and all images in (a) have the same scale. In (a), four consecutive images captured at the 2.5-cm measurement position show the sequence of bubble collapse, jetting, and beading resulting in new, single-phase particles. In (b), six other examples demonstrate the frequency with which this mechanism was observed. *Top row, from left:* 6.702 ms at 10 cm, 5.122 ms at 20 cm. *Bottom row, from left:* 3.399 ms at 2.5 cm, 6.319 ms at 10 cm, 10.436 ms at 20 cm, 13.500 ms at 30 cm.

4.3 Effect of Reaction/Expansion Mechanism on Particle Size

The preceding discussion considered the morphology of very large ($> 200 \mu\text{m}$) particles and why the median particle size decreases toward late times (Fig. 6). While large particles make up the majority of the reaction products, they are not observed *immediately* after ignition. Rather, Fig. 6 shows that the first particles observed are always much smaller, with the particle size increasing up to the maximum size over the first 0.5 – 5.0 ms. This behavior is directly correlated with the two distinct luminous zones

observed in the optical high-speed video (Fig. 4). As noted initially in Sec. 4.1, the leading Zone 1 expands and cools more quickly than the trailing Zone 2. To highlight this behavior, Fig. 10 shows linear intensity profiles measured along the tube axis during the first 12.5 ms after ignition. Zone 1 is visible as a separate peak in intensity running out toward the right, while the remaining, more slowly expanding peak constitutes Zone 2.

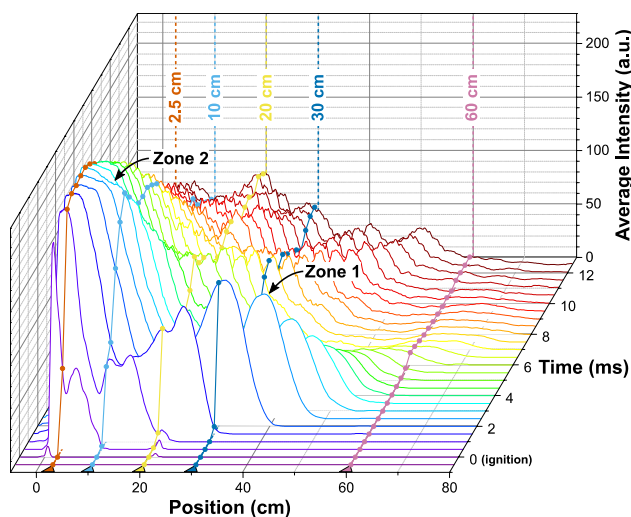


Fig. 10. Distribution of luminous intensity along the burn tube during the first 12.5 ms after ignition (curves spaced 0.5 ms in time). For clarity, data were smoothed using a simple adjacent-averaging scheme. The two reaction zones are labeled. Also plotted (perpendicular to the intensity curves) are the temporal variations in intensity at each measurement position.

Comparing Fig. 10 to Fig. 6, we find that the arrival of Zone 2 at a measurement position coincides fairly reliably with the end of the particle size ramp. In ascending order of measurement position, this arrival is at roughly 1.0 ms, 3.0 ms, 5.0 ms, 7.0 ms, and 12.5 ms in Fig. 10. These are a good match to the times at which the maximum median particle size is reached for each measurement position in Fig. 6. Given this correspondence, it is reasonable to conclude that Zone 1 consists of the smaller particles that are observed first, while Zone 2 corresponds to the “full-size” particles. This conclusion is also consistent with the observation that Zone 1 appears more diffuse and cools faster than Zone 2. The mechanism proposed to explain these two zones must thus also explain why the smallest particles are observed first.

The two distinct zones are observed almost immediately after ignition. After the particles begin flying down the tube, they will not spontaneously organize into zones spanning tens of centimeters. This

suggests that the variation arises solely from the ignition process and the portion of the reaction that occurs when the particles are still in a loose compact. Particle flow in the extended burn tube is one-directional, so the order of the luminous zones (i.e. small particles ahead of large) must correspond to the position of the original thermite in the particle bed. Ignition is at the far left in Figs. 4 and 10, so the thermite in Zone 1 is made up of the material that is initially farthest from the ignition point, while the thermite in Zone 2 originates closer to the ignition point. Clearly the thermite in Zone 2 must ignite before that in Zone 1, but physically, the thermite in Zone 2 is constrained and cannot expand into the tube until the thermite in front of it (Zone 1) does. In other words, the material in Zone 2 ignites *earlier* and expands *later* than the material in Zone 1. Since the initial reactants are nano-sized, there is a strong driving force for their coalescence as soon as this is kinetically feasible; if the particles cannot disperse before either reactant reaches its melting point, rapid, spontaneous consolidation will occur. The thermite in Zone 2 is most susceptible to this effect because it ignites first and expands last. In contrast, the material close to the edge of the particle bed (Zone 1) ignites late and experiences minimal resistance to expansion. Thermite in this region can leave the particle bed in response to a comparatively small gas release, minimizing consolidation. Within Zone 1, particles closer to the ignition point are ignited earlier, finish reacting earlier, and begin cooling earlier. This gives rise to the distinct “dark region” between Zones 1 and 2. This region still contains particles, they are just the first particles to finish reacting and cool.

This reaction/expansion mechanism is summarized schematically in Fig. 11 for an idealized cylindrical thermite charge. Ignition occurs at the back and the reaction propagates forward. Throughout most of this process, inertia prevents the thermite from expanding significantly as indicated by the lack of motion of lines A and B. When the flame front reaches a position close to the end of the bed, marked schematically by line A, the thermite begins to expand. Thermite ignited to the right of line A is able to expand on the same timescale as ignition, leading to relatively small particles (Zone 1). In contrast, the thermite ignited earlier (left of line A) undergoes consolidation before it expands and consequently forms

relatively large particles (Zone 2). While a cylindrical charge is a reasonable assumption for the burn tube, the proposed mechanism should apply to any ignition configuration where the directions of reaction propagation and thermite expansion are aligned.

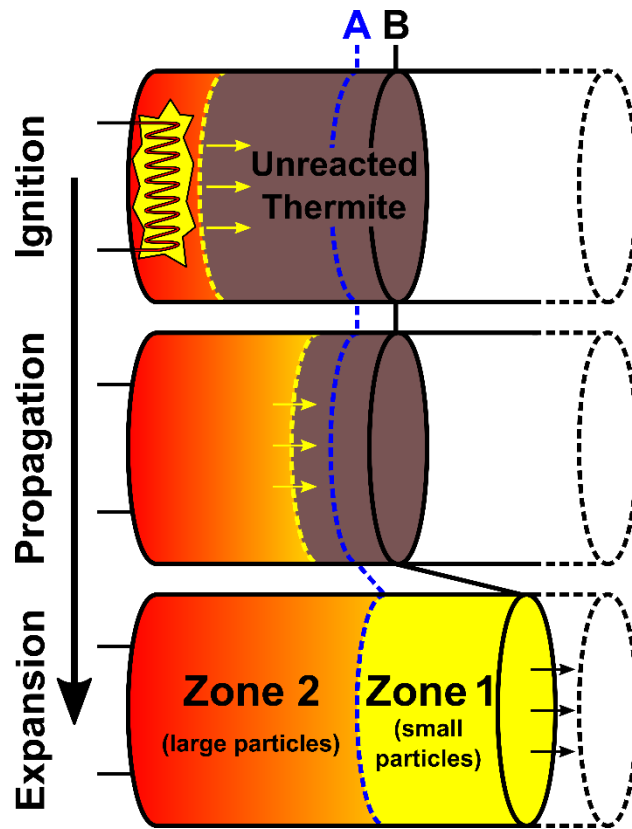


Fig. 11. Schematic depiction of a reaction and expansion process that could lead to two discrete reaction zones. Inertial effects prevent the thermite from expanding until propagation is nearly complete, causing most of the thermite (Zone 2) to consolidate and then expand as relatively large particles. Only a small fraction of the thermite particles (Zone 1) closest to the edge of the bed remain relatively small.

Fig. 6 shows that the transition between reaction zones rapidly becomes diffuse as the thermite expands. However, at the earliest measurement position (2.5 cm) we still observe a relatively abrupt increase in median particle size about 0.5 ms after ignition. This is consistent with the luminous intensity data shown in Figs. 4 and 10, which shows Zone 1 passing the 2.5-cm measurement position just before 0.5 ms after ignition. An examination of the x-ray images from around this time (Fig. 12) provides additional support for the mechanism proposed in Fig. 11. The first two frames (0.335 – 0.383 ms) show a field occupied only by small particles, while in the last two frames (0.527 – 0.574 ms) the median particle

size has increased significantly. In between (0.431 – 0.479 ms) a distinct particle “front” is seen crossing the field of view. This front seems to mark the transition from Zone 1 to Zone 2.

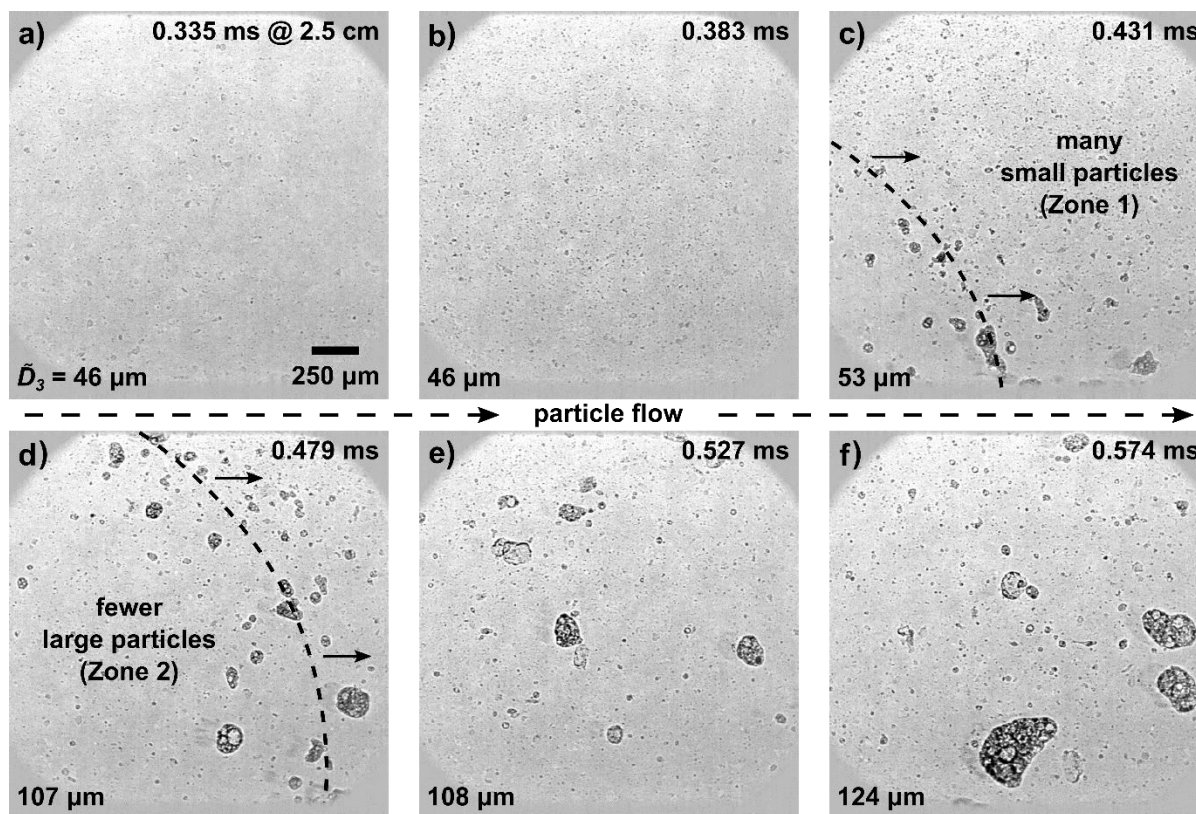


Fig. 12. Six consecutive frames from x-ray measurements taken 2.5 cm from the ignition point, showing the transition from small particles (Zone 1) to large particles (Zone 2). The dashed line in (c) and (d) indicates the approximate position of the observed particle “front” that delineates these two stages. The volume-median particle diameter from Fig. 6 is shown in the lower left of each frame.

The invocation of rapid coalescence to explain the observed variation in dynamic particle size is consistent with previous *in situ* observations of the Al/Fe₂O₃ reaction [24] which showed coalescence and the formation of large (5 – 50 μm) gas-filled bubbles on extremely short timescales (~ 44 μs). The thermite in that experiment was a < 100 μm film coated on a hot wire and thus experienced minimal confinement. It is not surprising that, with the addition of self-confinement in the burn tube geometry, composite particles even larger than those observed during hot wire ignition are formed. We anticipate that this early time coalescence could be somewhat mitigated, although not entirely eliminated, by moving from hot wire ignition to something like shock initiation [3,17]. This would both increase the heating rate and promote rapid dispersion of the thermite, both of which would reduce the opportunity for coalescence to occur.

4.4 Dynamic Particle Size and Burn Time

Having explored some of the details of the hot particles in these experiments, it is interesting to take a step back and consider the burn tube experiment from the perspective of macroscopic luminous intensity and burn time as summarized in Fig. 5. In particular, we are interested in how the underlying particle dynamics relate to the luminous intensity observed at the macro scale, and whether any subset of the insights gained could now be inferred from luminous intensity alone. The Al/Fe₂O₃ formulation, with its two distinct reaction zones, presents a convenient test case. Knowing that Zone 1 consists of relatively small particles while the particles of Zone 2 are much larger, we can analyze the burn time in these two zones independently and see whether the measured differences are consistent with the measured particle sizes. In particular, the trailing half-width burn time (associated with the rate at which the reaction products cool) should be longer for Zone 2 since large particles have proportionally less surface area to volume. While the x-ray measurements were unable to resolve the specifics of the thermite reaction itself, the leading half-width burn time can be used to assess whether the observed consolidation alters the effective reaction length scale.

Table I lists the FWHM and leading/trailing half-width burn times for the reaction as a whole, Zone 1 only, and Zone 2 only. As expected, the trailing half-width for the Zone 2 reaction is significantly longer than the trailing half-width for Zone 1. This is qualitatively consistent with the x-ray measurements, which show that the median particle size in Zone 2 is much larger than that of Zone 1. The leading half-width for Zone 2 is also longer than for Zone 1, suggesting that particle coalescence may be happening on a short enough timescale to increase the effective reactant spacing and reduce the effective reaction rate. However, this may also be an artifact of the larger volume of thermite in Zone 2 since any variation in ignition time tends to broaden the luminous signal.

Table I. FWHM and component burn times measured globally (for the entire tube), for Zone 1 only, and for Zone 2 only. Each value is an average for the five experiments performed. The measured differences between zones are consistent with our expectations based on the difference in particle sizes making up each zone.

	Global	Zone 1	Zone 2
Leading Half-Width (ms)	2.7 ± 0.7	0.4 ± 0.3	1.7 ± 0.4
Trailing Half-Width (ms)	9 ± 2	1.6 ± 0.7	8 ± 2
Full-Width at Half Maximum (ms)	12 ± 2	2 ± 1	10 ± 1

These results suggest that luminous intensity measurements, common experiments that can be performed in any laboratory, can be used directly to make inferences about the underlying particle dynamics that make up the reaction. They also highlight the importance of looking beyond a simple global FWHM measurement of burn time. Analyzing rising and trailing burn times separately and considering the spatial distribution of intensity (whether in discrete zones or continuously as in Fig. 10) are all approaches that can yield useful information beyond what is implied by a single FWHM burn time.

4.5 Burn Time as a Measure of Reactivity

While measuring burn time may allow us to ignore the effects of thermal transport, the data presented in Table I demonstrate that it can still be biased by factors other than the intrinsic chemical reaction kinetics. The trailing half-width makes up 70 – 80% of the FWHM. Our results show that trailing half-width burn time is strongly linked to particle size and particle size is determined by how the thermite expands after it is ignited. That means that the apparent FWHM burn time is sensitive not only to reaction kinetics but also to the expansion mechanism. Thermite formulations that generate more gas or release gas earlier in the reaction will tend to expand more quickly and be less susceptible to reactive coalescence, yielding smaller particles. By the above reasoning, these formulations should also have a shorter FWHM burn time and, in a typical analysis, ultimately be classified as “more reactive”. Interestingly, these same thermites are also likely to be classified as more reactive on the basis of propagation rate, since gas release promotes rapid convective heat transfer.

While this consistency is encouraging, it is important to remember that the reactivity assessed in this way is not necessarily indicative of the intrinsic chemical reaction rate and tends to favor one particular type of formulation: strong gas generators. The availability of other burn time “components” to describe burn tube experiments may allow more targeted optimizations in the future. If an application requires a thermite that rapidly heats, disperses, *and* cools, then selecting an optimal formulation on the basis of minimum FWHM burn time may indeed be the right approach. However, if just the thermal rise time is important, a metric like leading half-width can be used instead since it is not biased by variations in cooling kinetics. One might even consider optimizing the trailing half-width if the goal was a thermite that stayed hot as long as possible, e.g. to maximize energy on target.

As highlighted in the introduction, many parameters are available to perform this optimization using formulation alone. However, other approaches are also conceivable based on the insights gained here. If a thermite that stays hot for a long time is desired, varying levels of additional confinement (beyond the “self confinement” described in this paper) could be explored that would further delay expansion and allow the thermite to sinter into larger particles. If in contrast the focus is on rapid energy release, it may be possible to promote this by the addition of heat-activated “dispersants” that would contribute additional early-time gas release to the reaction and help to disperse the thermite before coalescence occurs. Published results showing the combination of nitrocellulose with Al/CuO thermite seem to support the idea that the addition of gas-generating materials to thermites can promote reaction [34]. Identifying and exploring methods to either mitigate or promote particle coalescence early in the reaction may become an important avenue for tailoring performance.

5. Conclusions

We have obtained high-resolution, time-resolved images of Al/Fe₂O₃ thermite reacting in an extended burn tube experiment. Advanced image processing algorithms have been developed to extract a continuous record of composite particle size as a function of time and distance from the ignition point.

In general, the observed thermite reaction products are large, multi-phase composite particles. The particle size tends to decrease over time, and two particle size refinement mechanisms have been identified, both based on the collapse of large gas bubbles. Small particles are also observed immediately after ignition. Based on correlations between the time-varying particle size and the visible light emission from the reaction, a two-stage reaction/expansion mechanism is proposed, where thermite closest to the ignition point expands in a more consolidated state (i.e. larger particles) than the thermite farthest away. Finally, we have shown that a more nuanced concept of burn time that takes into account the skew in the luminous intensity may be a way to improve reactivity assessments in the absence of *in situ* data. While the spatial and temporal resolution of the experiments reported here represent a significant advancement over prior work, continued development will be needed if the ultimate goal is to extract data on the intrinsic kinetics of the thermite reaction.

Acknowledgements

The authors would like to thank T. Willey (LLNL) for his assistance in planning and designing the synchrotron experiments. The efforts of M.D.G, R.V.R, J.M.D, and K.T.S. were supported by the LLNL Laboratory-Directed Research and Development program under project number 16-FS-028. This research used resources of the Advanced Photon Source, a U.S. Department of Energy (DOE) Office of Science User Facility operated for the DOE Office of Science by Argonne National Laboratory under Contract DE-AC02-06CH11357. This work was performed under the auspices of the U.S. DOE by Lawrence Livermore National Laboratory under Contract DE-AC52-07NA27344. Document release number LLNL-JRNL-752112.

Disclaimer

This document was prepared as an account of work sponsored by an agency of the United States government. Neither the United States government nor Lawrence Livermore National Security, LLC, nor any of their employees makes any warranty, expressed or implied, or assumes any legal liability or

responsibility for the accuracy, completeness, or usefulness of any information, apparatus, product, or process disclosed, or represents that its use would not infringe privately owned rights. Reference herein to any specific commercial product, process, or service by trade name, trademark, manufacturer, or otherwise does not necessarily constitute or imply its endorsement, recommendation, or favoring by the United States government or Lawrence Livermore National Security, LLC. The views and opinions of authors expressed herein do not necessarily state or reflect those of the United States government or Lawrence Livermore National Security, LLC, and shall not be used for advertising or product endorsement purposes.

References

- [1] S.H. Fischer, M.C. Grubelich, A survey of combustible metals, thermites, and intermetallics for pyrotechnic applications, 32nd Jt. Propuls. Conf. Exhib., American Institute of Aeronautics and Astronautics (1996).
- [2] K.T. Sullivan, N.W. Piekielek, S. Chowdhury, C. Wu, M.R. Zachariah, C.E. Johnson, Ignition and Combustion Characteristics of Nanoscale Al/AgIO₃: A Potential Energetic Biocidal System, *Combust. Sci. Technol.* 183 (2010) 285–302.
- [3] B.A. Mason, L.J. Groven, S.F. Son, R.A. Yetter, Combustion Performance of Several Nanosilicon-Based Nanoenergetics, *J. Propuls. Power.* 29 (2013) 1435–1444.
- [4] V.E. Sanders, B.W. Asay, T.J. Foley, B.C. Tappan, A.N. Pacheco, S.F. Son, Reaction Propagation of Four Nanoscale Energetic Composites (Al/MoO₃, Al/WO₃, Al/CuO, and Bi₂O₃), *J. Propuls. Power.* 23 (2007) 707–714.
- [5] M.R. Weismiller, J.Y. Malchi, J.G. Lee, R.A. Yetter, T.J. Foley, Effects of fuel and oxidizer particle dimensions on the propagation of aluminum containing thermites, *Proc. Combust. Inst.* 33 (2011) 1989–1996.
- [6] M.L. Pantoya, J.J. Granier, Combustion Behavior of Highly Energetic Thermites: Nano versus Micron Composites, *Propellants, Explos. Pyrotech.* 30 (2005) 53–62.
- [7] K.T. Sullivan, J.D. Kuntz, A.E. Gash, The Role of Fuel Particle Size on Flame Propagation Velocity in Thermites with a Nanoscale Oxidizer, *Propellants, Explos. Pyrotech.* 39 (2014) 407–415.
- [8] K.B. Plantier, M.L. Pantoya, A.E. Gash, Combustion wave speeds of nanocomposite Al/Fe₂O₃: the effects of Fe₂O₃ particle synthesis technique, *Combust. Flame.* 140 (2005) 299–309.
- [9] G.M. Dutro, R.A. Yetter, G.A. Risha, S.F. Son, The effect of stoichiometry on the combustion behavior of a nanoscale Al/MoO₃ thermite, *Proc. Combust. Inst.* 32 (2009) 1921–1928.
- [10] B.S. Bockmon, M.L. Pantoya, S.F. Son, B.W. Asay, J.T. Mang, Combustion velocities and propagation mechanisms of metastable interstitial composites, *J. Appl. Phys.* 98 (2005) 64903.
- [11] K.T. Sullivan, M.A. Worsley, J.D. Kuntz, A.E. Gash, Electrophoretic deposition of binary energetic composites, *Combust. Flame.* 159 (2012) 2210–2218.
- [12] V.S. Parimi, S.A. Tadigadapa, R.A. Yetter, Control of nanoenergetics through organized microstructures, *J. Micromechanics Microengineering.* 22 (2012) 055011.
- [13] K.T. Sullivan, C. Zhu, E.B. Duoss, A.E. Gash, D.B. Kolesky, J.D. Kuntz, J.A. Lewis, C.M. Spadaccini, Controlling Material Reactivity Using Architecture, *Adv. Mater.* 28 (2016) 1934–1939.
- [14] J.M. Densmore, K.T. Sullivan, A.E. Gash, J.D. Kuntz, Expansion Behavior and Temperature Mapping of Thermites in Burn Tubes as a Function of Fill Length, *Propellants, Explos. Pyrotech.* 39 (2014) 416–422.
- [15] M.L. Pantoya, V.I. Levitas, J.J. Granier, J.B. Henderson, Effect of Bulk Density on Reaction Propagation in

Nanothermites and Micron Thermites, *J. Propuls. Power.* 25 (2009) 465–470.

- [16] B.W. Asay, S.F. Son, J.R. Busse, D.M. Oschwald, Ignition Characteristics of Metastable Intermolecular Composites, Propellants, Explos. Pyrotech. 29 (2004) 216–219.
- [17] T. Bazyn, N. Glumac, H. Krier, T.S. Ward, M. Schoenitz, E.L. Dreizin, Reflected shock ignition and combustion of aluminum and nanocomposite thermite powders, *Combust. Sci. Technol.* 179 (2007) 457–476.
- [18] I. Monk, M. Schoenitz, E.L. Dreizin, Modes of Ignition of Powder Layers of Nanocomposite Thermites by Electrostatic Discharge, *J. Energ. Mater.* 35 (2017) 29–43.
- [19] W.L. Shaw, D.D. Dlott, R.A. Williams, E.L. Dreizin, Ignition of Nanocomposite Thermites by Electric Spark and Shock Wave, *Propellants, Explos. Pyrotech.* 39 (2014) 444–453.
- [20] K.T. Sullivan, O. Cervantes, J.M. Densmore, J.D. Kuntz, A.E. Gash, J.D. Molitoris, Quantifying Dynamic Processes in Reactive Materials: An Extended Burn Tube Test, *Propellants, Explos. Pyrotech.* 40 (2015) 394–401.
- [21] K.T. Sullivan, M.R. Zachariah, Simultaneous Pressure and Optical Measurements of Nanoaluminum Thermites: Investigating the Reaction Mechanism, *J. Propuls. Power.* 26 (2010) 467–472.
- [22] M.W. Beckstead, A Summary of Aluminum Combustion, Spec. Course Intern. Aerodyn. Solid Rocket Propuls., NATO Research & Technology Office and von Karman Institute for Fluid Dynamics (2004).
- [23] T. Bazyn, H. Krier, N. Glumac, Evidence for the transition from the diffusion-limit in aluminum particle combustion, *Proc. Combust. Inst.* 31 (2007) 2021–2028.
- [24] K.T. Sullivan, N.W. Piekielek, C. Wu, S. Chowdhury, S.T. Kelly, T.C. Hufnagel, K. Fezzaa, M.R. Zachariah, Reactive sintering: An important component in the combustion of nanocomposite thermites, *Combust. Flame.* 159 (2012) 2–15.
- [25] K.T. Sullivan, W.-A. Chiou, R. Fiore, M.R. Zachariah, In situ microscopy of rapidly heated nano-Al and nano-Al/WO₃ thermites, *Appl. Phys. Lett.* 97 (2010) 133104.
- [26] G.C. Egan, T. LaGrange, M.R. Zachariah, Time-Resolved Nanosecond Imaging of Nanoscale Condensed Phase Reaction, *J. Phys. Chem. C.* 119 (2015) 2792–2797.
- [27] C.P. Lonsdale, Thermite rail welding: history, process developments, current practices and outlook for the 21st century, *Proc. AREMA 1999 Annu. Conf., American Railway Engineering and Maintenance-of-Way Association* (1999).
- [28] M. Borland, G. Decker, L. Emery, W. Guo, K. Harkay, V. Sajaev, C.-Y. Yao, Storage Ring Operation Modes, APS Storage Ring Parameters, <https://ops.aps.anl.gov/SRparameters/node5.html> (2010).
- [29] C.A. Schneider, W.S. Rasband, K.W. Eliceiri, NIH Image to ImageJ: 25 years of image analysis, *Nat. Methods.* 9 (2012) 671–675.
- [30] L.-K. Huang, M.-J.J. Wang, Image thresholding by minimizing the measures of fuzziness, *Pattern Recognit.* 28 (1995) 41–51.
- [31] Y. Shoshin, E. Dreizin, Particle combustion rates in premixed flames of polydisperse metal - Air aerosols, *Combust. Flame.* 133 (2003) 275–287.
- [32] A.V. Grosse, A.D. Kirshenbaum, The densities of liquid iron and nickel and an estimate of their critical temperature, *J. Inorg. Nucl. Chem.* 25 (1963) 331–334.
- [33] B. Glorieux, F. Millot, J.-C. Rifflet, J.-P. Coutures, Density of Superheated and Undercooled Liquid Alumina by a Contactless Method, *Int. J. Thermophys.* 20 (1999) 1085–1094.
- [34] S. Yan, G. Jian, M.R. Zachariah, Electrospun Nanofiber-Based Thermite Textiles and their Reactive Properties, *ACS Appl. Mater. Interfaces.* 4 (2012) 6432–6435.